Sensorless Control of IM for Limp-Home Mode EV Applications

Ehsan Dehghan-Azad, *Student Member, IEEE*, Shady Gadoue, David Atkinson, Howard Slater, Peter Barrass, *Member, IEEE*, and Frede Blaabjerg, *Fellow, IEEE*

***Abstract*—This paper presents a novel speed estimation scheme for induction motors (IMs) based on back electromotive-force model reference adaptive system (back-EMF MRAS). The scheme is employed for the purpose of sensorless fault-tolerant torque-controlled drives used in a limp-home mode operation in electric vehicle (EV) applications. The proposed scheme was experimentally tested on a laboratory dynamometer using a 19-kW IM and a 29-kW controller, which are both currently used in the automotive industry for EV applications. The scheme was also implemented on an electric golf buggy which was equipped with a 5-kW IM. A performance comparison was carried out between the proposed and conventional back-EMF MRAS schemes for starting from standstill, sensitivity to parameter variations and constant speed operation with load variations. Utilizing the golf buggy, the behaviors of the new scheme was separately investigated for vehicle starting from standstill, wide speed range including field weakening region, and hill-starting operations. The proposed scheme is computationally easy to implement, robust against sensitivity to parameters variations, inverter nonlinearity and errors due to digitization in the field weakening region. This scheme is not only consistent for vehicle starting from standstill, it also provides a reliable vehicle-drive in the field weakening region and during vehicle hill-starting. The dynamometer and vehicle test-drive results show the suitability of the proposed scheme for the purpose of EV fault-tolerant limp-home mode operation.**

***Index Terms*—Electric vehicles (EVs), fault tolerant, induction motor (IM), model reference adaptive system (MRAS), sensorless, torque controlled-drive (TCD).**

I. Introduction

IN RECENT years, the electrificatio concept in the automotive industry has gained momentum as it promotes reduction in CO_2 emissions and lowers operating costs. Consequentially, electric vehicles (EVs) are becoming more popular choice over vehicles equipped with internal combustion engines. Popularity of EVs have prompted researchers to do further investigation in the functional safety of EV applications. By carrying out the failure mode and effect analysis for the electric drive used in an EV application, one would note that speed/position sensor failure can have catastrophic consequences, for instance, on a busy roundabout or highway. Although this failure may not have a high level of exposure classificatio in the automotive safety integrity level, the severity and controllability classification are very high. Therefore, it is critically important and required by the road vehicles-functional safety standards (ISO26262) for the drive mechanism, which is employed for EV applications, to be fault tolerant to the speed/position failure. The fault tolerant drive allows drivers and passengers of EVs to reach their destinations safely without disruption despite the occurrence of fault or failure [1], which is known as *limp-home* mode. Although in the *limp-home* mode, the EV's drive performance may experience degradation after sustaining a fault [2], this mode increases safety, reliability, and availability of the EV. The *limp-home* mode concept consists of a fault detection mechanism, a transition mechanism between sensored to sensorless control and vice versa, and more importantly, a robust and accurate speed/position estimator. In EV applications, high computational effort is already required to implement various control schemes, this is to achieve the functional safety which is a critical aspect. Therefore, because of the limited computational resources in the motor drive controller, the sensorless algorithm employed for fault tolerant purposes should not be too complicated.

For high performance applications, such as the EV and hybrid EV, torque controlled drives (TCDs) are usually employed for induction motors (IMs) [3]. From the point of view of EV applications, TCD based on fiel oriented control (FOC) is preferred over direct torque control (DTC). This is due to the well known major disadvantage of DTC which is high levels of torque and current ripples [4]–[7]. At very low speeds, when the vehicle is pulling away, these torque distortions create an undesirable cogging effect. For EVs in which the electric motor is coupled to a gearbox, torque ripples can excite gearbox oscillations which are very hard to dampen out. Utilizing FOC, rotor-flu angle calculation is required for transformation between stationary to synchronous reference frames and vice versa. The rotor-flu angle consists of the summation of slip and electrical rotor angles. If the speed/position signal is lost, due to sensor failure, the electrical rotor angle is estimated using a sensorless speed/position estimator scheme. In the literature, the concept of sensorless control for IM drives has been introduced for

Manuscript received May 29, 2016; revised September 9, 2016; accepted October 31, 2016. Date of publication November 10, 2016; date of current version April 24, 2017. Recommended for publication by Associate Editor Prof. S. Williamson.

E. Dehghan-Azad and D. Atkinson are with the School of Electrical and Electronic Engineering, Newcastle University, Newcastle Upon Tyne NE1 7RU, U.K. (e-mail: e.dehghan-azad@newcastle.ac.uk; dave.atkinson@ncl.ac.uk).

S. Gadoue is with the School of Electrical and Electronic Engineering, Newcastle University, Newcastle Upon-Tyne NE1 7RU, U.K. and also with Department of Electrical Engineering, Faculty of Engineering, Alexandria University, Alexandria 21544, Egypt (e-mail: shady.gadoue@ncl.ac.uk).

H. Slater and P. Barrass are with Sevcon Ltd., Gateshead NE11 0QA, U.K. (e-mail: howard.slater@sevcon.com; peter.barrass@sevcon.com).

F. Blaabjerg is with The Institute of Energy Technology, Aalborg University, Aalborg DK-9220, Denmark (e-mail: fbl@et.aau.dk).

Color versions of one or more of the f gures in this paper are available online at http://ieeexplore.ieee.org.

Digital Object Identifie 10.1109/TPEL.2016.2627685

the following reasons; cost reduction, cable elimination, noise reduction, and increased reliability [8]. Assorted sensorless speed estimation techniques have been investigated in literature [9]–[16], including; extended Kalman filte [9], sliding mode observer [10], [11], model reference adaptive system (MRAS) [12], [13], adaptive full-order observer [16], and artificia neural networking-based methods [14], [15]. Among the aforementioned techniques, schemes based on the MRAS are known for being simpler and requiring relatively lower computational effort [17], [18]. These MRAS schemes differ from one another by the way the error signal is calculated. These are; rotor-flux based MRAS (RF-MRAS) [19], back-electromotive force-based MRAS (Back-EMF MRAS) [20], [21], reactive power-based MRAS (RP-MRAS) [21], and stator current-based MRAS (Is-MRAS) [22].

The RF-MRAS suffers from dc drift problems associated with pure integration and sensitivity to stator resistance variation, especially in the low speed region [13], [23], [24]. In order to improve the performance of the RF-MRAS in the low speed region, second adaptation mechanism, based on electromagnetic torque was proposed in [25], which is added to the adaptation mechanism of the RF-MRAS. Although it has been shown in [25] that this approach improves the performance of the classical RF-MRAS at low speed, this scheme remains effected by the sensitivity to parameter variations. In [26], to improve stability of the RF-MRAS, a sliding mode stator voltage model observer is applied as the reference model. This approach introduces chattering on the torque response which is undesirable for EV applications. The RP-MRAS scheme is immune from sensitivity to stator resistance variations, however, it has stability problems in regenerating mode [20]. The Is-MRAS, proposed in [22], shows a good performance for a wide speed range. In this scheme, the error tuning signal is calculated using the error between the measured and the estimated stator currents which is then multiplied by the estimated rotor flu components. Consequently, the proposed scheme in [22], remains affected by the sensitivity to the motor parameter variations. In [27], a comparative study was carried out between modifie RF-MRAS and modifie Back-EMF MRAS. In the modifie schemes, two first order low-pass filte blocks have been inserted into the output and input of the reference and adjustable models, respectively. The study concluded that the adaptation gain constants of the modifie RF-MRAS is easier to design. However, the performance of the modifie Back-EMF MRAS is much better than the RF-MRAS at low speed region. Another comparative study in [28] also concluded that the Back-EMF MRAS has better tracking capability and it fulfill the requirement as a versatile estimator. In order to make the Back-EMF MRAS immune to the stator resistance variations, a combined speed and stator resistance estimators were proposed in [20] to operate simultaneously. The new combined scheme is reported to improve the stability of the Back-EMF MRAS and increase its robustness against the stator resistance mismatch. However, during a speed transient and no-load condition this scheme suffers from drift problems and it increases complexity compared to the conventional scheme. Although utilizing the Back-EMF MRAS would eliminate challenges related to pure integration in the reference model of the RF-MRAS, sensitivity to parameters variations remains unsolved [13].

Apart from challenges related to sensitivity to parameters variations, there are other factors which may affect the performance and stability of the Back-EMF MRAS scheme. For example, the inverter nonlinearity (e.g., switching dead-time and voltage drop of power semiconductor devices) causes voltage errors between the stator reference and actual input voltages of IM. At very low speed, these errors can even become larger than the motor's stator voltage [29], which can have serious effect on the performance of the Back-EMF MRAS in the low-speed region. Moreover, digitization effects can cause phase error in the reference model in the fiel weakening region [16], [30], which leads to the Back-EMF MRAS instability. In this paper, in order to deal with the aforementioned problems, a new Back-EMF MRAS scheme is proposed for the purpose of fault-tolerant *limp-home* mode operation in EV applications. The reference model of this scheme takes advantage of a novel compensating mechanism, to compensate for the errors due to parameter variations, inverter nonlinearity, and digitization in high-speed regions. A new approach is used in the adjustable model of this scheme which is also free from integration problems. This results in an effective sensorless control when starting from standstill and during high-speed operation. Experimental testing, based on a 19-kW IM and later on an electric golf buggy (powered with 5-kW IM), are carried out to investigate the performance of the proposed scheme. A realistic speed/torque profil is used for testing purposes. Experimental results demonstrate the robustness of this scheme against motor parameter variations in addition to successful starting from standstill. The vehicle test drive, utilizing the proposed scheme, confirm control stability and reliability during vehicle hill-starting and fiel weakening operation. The structure of this paper is as follows; Section II describes sensorless TCD using indirect rotor FOC (IRFOC) and a review of the fundamental concept of the conventional Back-EMF MRAS scheme. Section III gives a detailed description of the proposed scheme. Section IV describes the experimental system platform and Section V shows the experimental results of the proposed sensorless scheme. Finally the conclusion is provided in Section VI.

II. Sensorless Torque Controlled-Drive Based on IRFOC Using Back-EMF MRAS

A. Sensorless Torque Controlled-Drives Based on IRFOC Technique

The overall block diagram of the sensorless TCD based on IRFOC used in this paper for fault-tolerant EV application is shown in Fig. 1. In EV applications, the torque demand is applied by the driver using the accelerator pedal. In this approach, the reference stator current on the direct-axis (i_d^*) is kept constant below base speed. Normally, the sensorless speed/TCDs based on the FOC techniques which have been investigated in literature [31]–[33], consist of an outer speed/torque control feedback loop. This is used for the calculation of the reference stator current on the quadrature-axis (i_q^*) in the synchronous reference frame. Using the outer feedback loop at zero and low speeds,

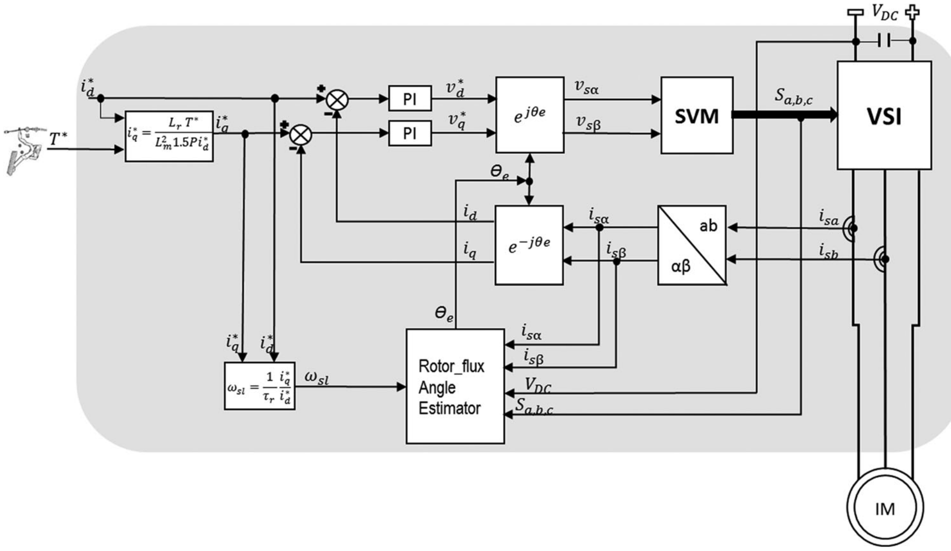

Fig. 1. Block diagram of sensorless TCD based on IRFOC.

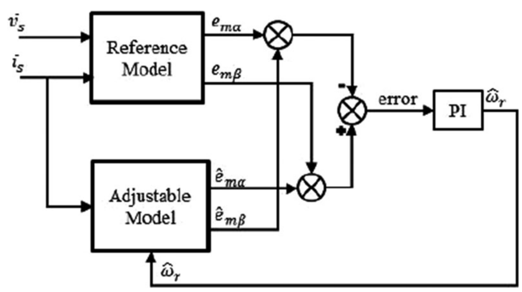

Fig. 2. Block diagram of the conventional back-EMF MRAS scheme.

where almost all of the sensorless schemes struggle or fail to estimate accurately, can lead to erroneous i_q^* calculation. As far as EV applications are concerned, correct drive direction to that requested in vehicle starting from standstill is critical. Therefore, by eliminating the outer feedback loop in sensorless TCDs, a precise i_q^* calculation can be achieved, which assists the drive with vehicle starting in the right direction from standstill.

B. Conventional Back-EMF MRAS Scheme

The block diagram of the conventional Back-EMF MRAS is shown in Fig. 2. For this scheme, measured stator currents and reconstructed stator voltage components in the stationary reference frame are required. The block diagram of MRAS schemes normally consist of a reference model, an adjustable model, and an adaptation mechanism. The conventional Back-EMF MRAS scheme utilizes the induced back-EMF components in the stationary reference frame for the reference and adjustable models.

The equations for the reference back-EMF components provided by the reference model can be derived from the IM stator voltage in the stationary reference frame as the following:

$$\begin{cases} v_{s\alpha} = R_s i_{s\alpha} + L_s \sigma p i_{s\alpha} + \dfrac{L_m}{L_r} p \psi_{r\alpha} \\ v_{s\beta} = R_s i_{s\beta} + L_s \sigma p i_{s\beta} + \dfrac{L_m}{L_r} p \psi_{r\beta} \end{cases} \tag{1}$$

where $v_{s\alpha\beta}$, $i_{s\alpha\beta}$, and $\psi_{r\alpha\beta}$ are stator voltage, current, and rotor flu linkage components in the stationary reference frame, respectively. R_s, L_s, L_m, and L_r are stator resistance, stator self, magnetizing, and rotor inductances, respectively. $p = \frac{d}{dt}$ is the differential operator and $\sigma = 1 - \left(\frac{L_m^2}{L_s L_r}\right)$ is the leakage coefficien of the machine.

In (1), $\left(\frac{L_m}{L_r} p \bar{\psi}_r\right)$ is the back-EMF term. Hence, the back-EMF of the IM in the stationary reference frame can be obtained by rearranging (1) as given below

$$\begin{cases} e_{m\alpha} = v_{s\alpha} - R_s i_{s\alpha} - L_s \sigma p i_{s\alpha} \\ e_{m\beta} = v_{s\beta} - R_s i_{s\beta} - L_s \sigma p i_{s\beta} \end{cases} \tag{2}$$

where $e_{m\alpha}$ and $e_{m\beta}$ are the reference back-EMF components in the stationary reference frame.

The equations for the estimated back-EMF components provided by the adjustable model can be written as the following:

$$\begin{cases} \hat{e}_{m\alpha} = \dfrac{L_m}{L_r} p \psi_{r\alpha} = \dfrac{L_m}{L_r} \dfrac{(L_m i_{s\alpha} - \psi_{r\alpha} - \hat{\omega}_r T_r \psi_{r\beta})}{T_r} \\ \hat{e}_{m\beta} = \dfrac{L_m}{L_r} p \psi_{r\beta} = \dfrac{L_m}{L_r} \dfrac{(L_m i_{s\beta} - \psi_{r\beta} + \hat{\omega}_r T_r \psi_{r\alpha})}{T_r} \end{cases} \tag{3}$$

where $\hat{e}_{m\alpha}$ and $\hat{e}_{m\beta}$ are the estimated back-EMF components in the stationary reference frame from the adjustable model. $T_r = \frac{L_r}{R_r}$ is the rotor time constant (where R_r is the rotor resistance) and $\hat{\omega}_r$ is the estimated electrical rotor angular velocity.

The estimated rotor angular velocity is obtained from the adaptation mechanism

$$\hat{\omega}_r = \left(k_p + \frac{k_i}{s}\right) * (\epsilon_\omega) \tag{4}$$

where k_p and k_i are proportional and integral gains, respectively, and $\epsilon_\omega = (\hat{e}_{m\alpha\beta} \otimes e_{m\alpha\beta})$ is the speed error tuning signal. The error tuning signal is calculated from the cross product ($\otimes$) of the estimated and the reference back-EMF components in the stationary reference frame.

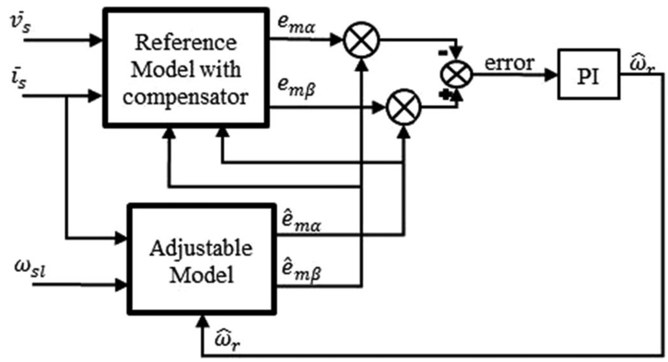

Fig. 3. Block diagram of the proposed back-EMF MRAS scheme.

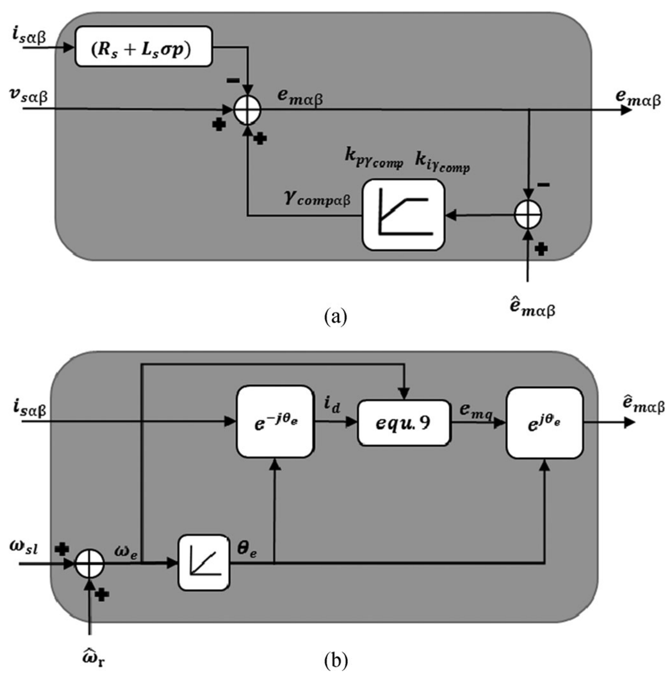

Fig. 4. Signal fl w diagrams of the proposed scheme; (a) reference model and (b) adjustable model.

III. Proposed Back-EMF MRAS Scheme

The block diagram of the proposed Back-EMF MRAS is shown in Fig. 3. The signal fl w diagrams of the reference and adjustable models of the proposed scheme are shown in Fig. 4(a) and (b), respectively. The reference model consists of two PI controllers which utilize errors between back-EMF components of the adjustable and reference models, to compensate for the errors due to the motor parameters variation, digitization, and inverter nonlinearity. The adjustable model is based on the back-EMF in the synchronous reference frame, hence the mutual cross coupling and rotor-flu integration in (3) is no longer required. This approach promotes increase in the stability of the MRAS schemes, due to being immune from problems related to the noise and offset accumulations caused by integration. The back-EMF components of the adjustable model are initially calculated in the synchronous reference frame and then transformed to the stationary reference frame. The back-EMF of IM can be expressed in the synchronous reference frame. This is achieved by firs transferring the stator voltage equations in (1) from stationary to synchronous reference frame

$$\begin{cases} v_{sd} = (R_s + L_s\sigma p)\, i_{sd} + \dfrac{L_m}{L_r} p\psi_{rd} \\ \qquad - \omega_e \left(L_s\sigma i_{sq} + \dfrac{L_m}{L_r}\psi_{rq} \right) \\ v_{sq} = (R_s + L_s\sigma p)\, i_{sq} + \dfrac{L_m}{L_r} p\psi_{rq} \\ \qquad + \omega_e \left(L_s\sigma i_{sd} + \dfrac{L_m}{L_r}\psi_{rd} \right) \end{cases} \tag{5}$$

where subscripts *d-q* represents variables in the synchronous reference frame. In the IRFOC, the rotor flu is aligned with the *d*-axis of the synchronous reference as

$$\psi_{rq} = 0, \text{ hence; } \psi_r = \psi_{rd} \tag{6}$$

where ψ_{rd} is the *d*-axis rotor flu which can be obtained by

$$\psi_{rd} = L_m\, i_{sd}. \tag{7}$$

Applying the IRFOC's law (6) in (5), they become

$$\begin{cases} v_{sd} = (R_s + L_s\sigma p)\, i_{sd} + \dfrac{L_m}{L_r} p\psi_{rd} - \omega_e L_s\sigma i_{sq} \\ v_{sq} = (R_s + L_s\sigma p)\, i_{sq} + \omega_e L_s\sigma i_{sd} + e_{mq} \end{cases} \tag{8}$$

where

$$e_{mq} = \omega_e \frac{L_m}{L_r}\psi_{rd}. \tag{9}$$

e_{mq} is back-EMF in the synchronous reference frame.

Note that the back-EMF term in the synchronous reference frame only appears on the *q*-axis. It is proportional to the rotor flu and the synchronous speed. The estimated back-EMF vector of the adjustable model is calculated by transforming (9) from the synchronous to the stationary reference frame

$$\begin{cases} \hat{e}_{m\alpha} = -\, e_{mq} * \sin(\theta_e) \\ \hat{e}_{m\beta} = e_{mq} * \cos(\theta_e) \end{cases} \tag{10}$$

where θ_e is angular position in the synchronous reference frame.

The back-EMF vector of the reference model in the stationary reference frame is calculated using the following:

$$\begin{cases} e_{m\alpha} = v_{s\alpha} - \left(R_s i_{s\alpha} + L_s\sigma \dfrac{d}{dt} i_{s\alpha} \right) + \gamma_{\mathrm{comp}\alpha} \\ e_{m\beta} = v_{s\beta} - \left(R_s i_{s\beta} + L_s\sigma \dfrac{d}{dt} i_{s\beta} \right) + \gamma_{\mathrm{comp}\beta} \end{cases} \tag{11}$$

where $\gamma_{\mathrm{comp}\alpha}$ and $\gamma_{\mathrm{comp}\beta}$ are the back-EMF compensating components. These are calculated utilizing PI controllers to drive the error between the back-EMF components of the adjustable and reference models to zero

$$\begin{cases} \gamma_{\mathrm{comp}_\alpha} = \left(k_{p\gamma_{\mathrm{comp}}} + \dfrac{k_{i\gamma_{\mathrm{comp}}}}{s} \right) \left(\epsilon_{\gamma_{\mathrm{comp}\alpha}} \right) \\ \gamma_{\mathrm{comp}_\beta} = \left(k_{p\gamma_{\mathrm{comp}}} + \dfrac{k_{i\gamma_{\mathrm{comp}}}}{s} \right) \left(\epsilon_{\gamma_{\mathrm{comp}\beta}} \right) \end{cases} \tag{12}$$

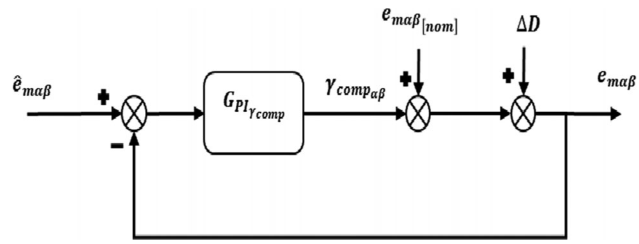

Fig. 5. Block diagram of the compensating mechanism.

where $\epsilon_{\gamma_{\text{comp}\alpha}} = \hat{e}_{m\alpha} - e_{m\alpha}$ and $\epsilon_{\gamma_{\text{comp}\beta}} = \hat{e}_{m\beta} - e_{m\beta}$ are the back-EMF error components used in the compensating mechanism. Fig. 5 shows a block diagram of the compensating mechanism. The term $e_{m\alpha\beta_{[nom]}}$ represents the nominal back-EMF components, calculated when nominal parameters of the IM are used. The term $e_{m\alpha\beta}$ represents the output back-EMF components of the reference model. The term ΔD represents disturbances due to parameter variations (ΔR_s and $\Delta L_s\sigma$), digitization, and inverter nonlinearity which can affect the reference model. Without the compensator, the output back-EMF components include the nominal back-EMF components plus some disturbances. These disturbances can cause a steady-state error, oscillation, and eventually lead to instability, especially in the low-speed region due to stator resistance variation and inverter nonlinearity. However, by closing the loop using the estimated back-EMF components from the adjustable model, which are free from aforementioned disturbances, the effects of ΔD can be eliminated.

The transfer function of feedback block diagram of the compensating mechanism with respect to the output back-EMF components and the control loop can be expressed by superposition of the response to the three inputs individually, as follows:

$$e_{m\alpha\beta_{cl}} = \frac{G_{PI_{\gamma_{\text{comp}}}}}{1 + G_{PI_{\gamma_{\text{comp}}}}}\,\hat{e}_{m\alpha\beta} + \frac{1}{1 + G_{PI_{\gamma_{\text{comp}}}}}\,e_{m\alpha\beta_{[\text{nom}]}} + \frac{1}{1 + G_{PI_{\gamma_{\text{comp}}}}}\,\Delta D\,. \tag{13}$$

The compensating mechanism is stable if all the poles of (13) are on the left-half plane. This can be investigated in the s-plane by setting the denominator to zero, which yields

$$\text{s} = -\frac{k_{i\gamma_{\text{comp}}}}{1 + k_{p\gamma_{\text{comp}}}}. \tag{14}$$

It can be seen that (14) is negative, hence, the compensator is stable. For the adaptation mechanism, a PI controller, similar to the one used for the conventional scheme in (4), is employed to minimize the speed error. To guarantee that the estimated rotor speed converges to the actual rotor speed, the overall proposed MRAS requires to be asymptotically stable. The overall stability of the proposed MRAS is investigated by employing a Lyapunov function V, which is expressed as below [25]

$$V = \bar{\epsilon}_{e_m}^T\,\bar{\epsilon}_{e_m} > 0 \tag{15}$$

where $\bar{\epsilon}_{e_m} = \begin{bmatrix} e_{m\alpha} - \hat{e}_{m\alpha} \\ e_{m\beta} - \hat{e}_{m\beta} \end{bmatrix}$ is error vector.

The state error equations can be expressed as below

$$\dot{\bar{\epsilon}}_{e_m} = [A][\bar{\epsilon}_{e_m}] - [W] \tag{16}$$

where

$$A = \begin{bmatrix} -1 & 0 \\ 0 & -1 \end{bmatrix},\ W = J\hat{e}_{m\alpha\beta}\left(\omega_r - \hat{\omega}_r\right),$$
$$J = \begin{bmatrix} 0 & -1 \\ 1 & 0 \end{bmatrix}. \tag{17}$$

Differentiating both side of (15), yields

$$\begin{aligned}\dot{V} &= \left(\dot{\bar{\epsilon}}_{e_m}^T\,\bar{\epsilon}_{e_m}\right) + \left(\bar{\epsilon}_{e_m}^T\,\dot{\bar{\epsilon}}_{e_m}\right) = \bar{\epsilon}_{e_m}^T\left(A^T + A\right)\bar{\epsilon}_{e_m} \\ &= -2\bar{\epsilon}_{e_m}^T\,\bar{\epsilon}_{e_m}\,.\end{aligned} \tag{18}$$

The function given in (18) is always negative. A system is said to be asymptotically stable if Lyapunov function satisfie following conditions [25], [34]:

$$\begin{cases} 1)\ V = 0 \text{ for } \hat{\omega}_r = 0 \\ 2)\ V > 0 \text{ for } \|\hat{\omega}_r\| \neq 0 \\ 3)\ \dot{V} \leq 0. \end{cases} \tag{19}$$

It is clear that (15) satisfie conditions 1 and 2 of (19), this is regardless of the estimated speed direction. Moreover, (18) also satisfie condition 3 of (19). Hence, it can be state that the proposed scheme is asymptotically stable.

IV. Experimental Setup

The proposed scheme was experimentally implemented and tested using a dynamometer (Dyno.) test bench which was built for the purpose of this experiment. In order to validate performance on actual EV, the scheme also was implemented and tested on an electric golf buggy. The block diagram of the overall setup, its photograph, and the golf buggy are shown in Fig. 6(a)–(c), respectively. The Dyno. test bench consists of a three-phase 19-kW IM loaded with a surface-mounted permanent magnet synchronous motor (SPMSM). It also consists of a 300 Nm torque transducer which was used for validation. Two 29-kW generation 4 (D8-Gen4) controllers were used for driving both motors. The D8-Gen4 controllers are equipped with 32-bit floatin point μ-processor, with sampling frequency of 16 kHz, and are capable of performing four quadrant control in the speed and torque modes. The stator currents were measured using two Hall sensors which are built in the controllers.

In order to communicate with the D8-Gen4 on the IM, device verificatio tool software was utilized. During experiments, the rotor speed was varied using speed throttle box connected to the D8-Gen4, which was controlling the SPMSM. The D8-Gen4 controller connected to the IM was set on the torque mode and the torque commands were applied using the laptop. The IM and SPMSM were equipped with an AB and a Sine/Cos encoders, respectively. These were used for evaluation of the implemented sensorless approach (measured speed). The sensorless control algorism was hand-coded in C-programming language and was compiled using "Keil" software development environment. The golf buggy also was equipped by a D8-Gen4 and a three-phase 5-kW IM. The nominal parameters of both IMs are provided in Appendix.

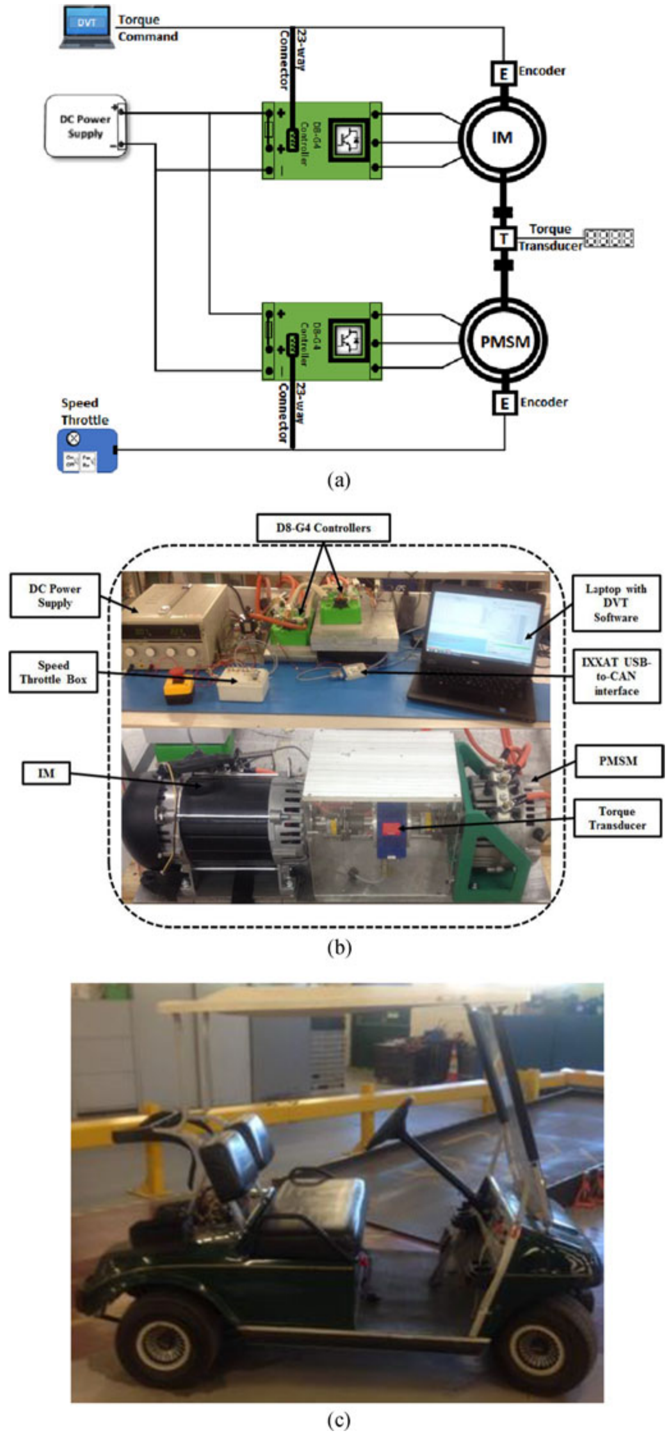

Fig. 6. Experimental setups; (a) overall block diagram, (b) actual test bench, and (c) golf buggy.

V. Experimental Results and Discussion

In this section, experimental results and discussion are presented to evaluate the effectiveness and feasibility of the proposed scheme for different operating conditions. Using the test bench, the performance of the proposed scheme was compared against that of the conventional Back-EMF MRAS scheme. All of the experiments were conducted in the sensorless mode with the reference d-axis stator current set to a constant value ($i_d^* = 52$ A). The controller has achieved software loop time 62.5 μs, bandwidth of 160 rad/s, gain margin of 25.4 db, and phase margin of 70º. For experiments using the golf buggy, the value of the reference d-axis stator current was produced using a Lookup Table. This was to allow the vehicle to function in the whole speed range. For these tests, the measured (encoder) and estimated (sensorless) speeds were recorded. In order to tune the estimator PI controller gains of the proposed scheme, the identical compensator PI controllers gains were initially set to zero. To obtain the optimal dynamic performance, the adaptation PI controller gains were firs tuned, while the encoder signal was used for the transformation between reference frames. The proportional gain of the adaptation PI controller was gradually increased, while the integral gain was set to zero, until the estimator speed could approximately track the actual speed. Then, the integral gain was increased to achieve faster dynamic response. After aforementioned procedure for the proposed scheme, both gains of the compensator PI controllers were set to one. This results in a small steady-state error between the actual and estimated speed. By gradually decreasing both gains, the error is reduced to zero. We have found that the dynamic performance of the compensator PI controllers are more dependent on the proportional gain than the integral gain. Therefore, the integral gain can be set to any value smaller than one, as long as it is greater than zero.

Utilizing the above procedure, for experiments on the Dyno. test bench, the adaptation PI controller gains of the conventional and proposed schemes were set to ($K_p = 1$ and $K_i = 0.1$) and ($K_p = 0.8$ and $K_i = 0.08$), respectively. The gains of the compensator PI controllers in the reference model of the proposed scheme were set to ($k_{p\gamma_{\text{comp}}} = 0.1$ and $k_{i\gamma_{\text{comp}}} = 0.001$). For experiments on the golf buggy, the adaptation PI controller gains of the proposed schemes were set to ($K_p = 0.9$ and $K_i = 0.08$). The gains of the compensator PI controllers in the reference model of the proposed scheme were set to ($k_{p\gamma_{\text{comp}}} = 0.1$ and $k_{i\gamma_{\text{comp}}} = 0.002$).

A. Experimental Results From Test Bench

1) Starting From Standstill: The sensorless IM TCD used for the purpose of fault-tolerant *limp-home* mode of EV applications must be capable of performing adequately at zero and low speeds.

It is also very important to have consistency in performing vehicle starting from standstill for consecutive attempts. Therefore, this test was carried out for three consecutive attempts in forward direction to demonstrate the consistency of the conventional and the proposed Back-EMF MRAS schemes for starting from standstill. During this test, the speed is varied using the throttle box with the applied torque command kept at 15 Nm. Fig. 7(a) shows the result of this test for the conventional scheme. Since, in the firs attempt, the conventional scheme had failed to start from standstill for an applied torque command of 15 Nm, the torque command was increased to 20 and 25 Nm for the second and third attempts, respectively. From result of the proposed scheme, which is shown in Fig. 7(b), it is clear that

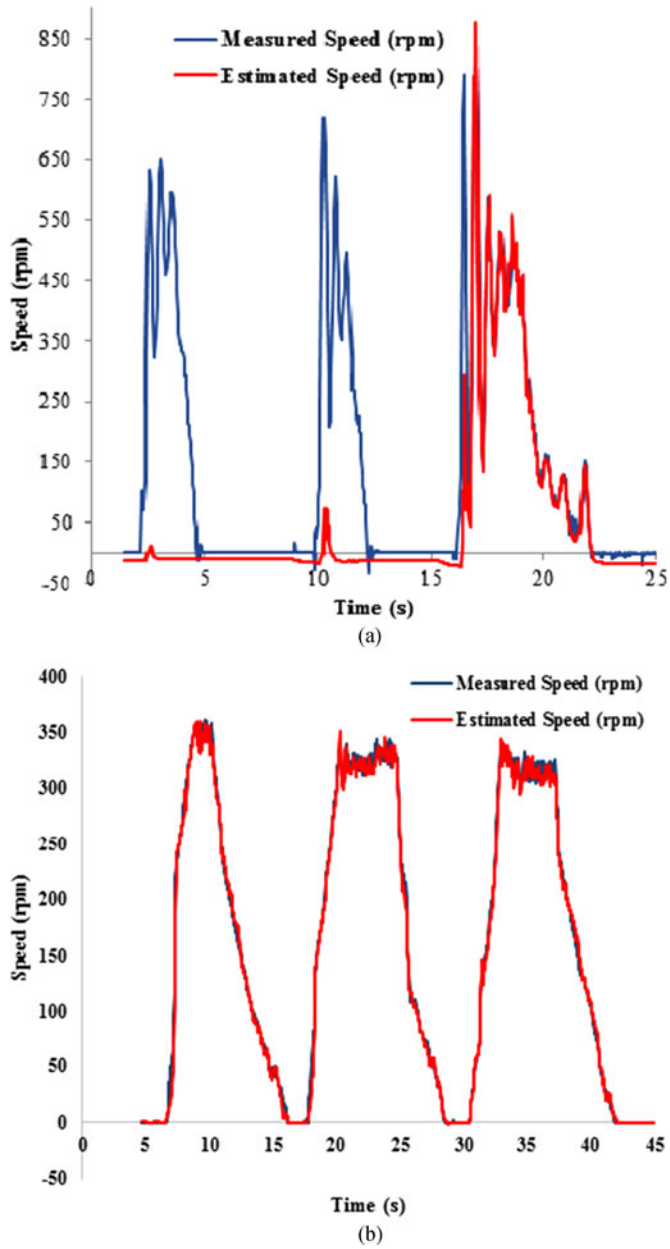

Fig. 7. Experimental results for sensorless performance starting from standstill with nominal parameters at 15 Nm. (a) Conventional Back-EMF MRAS (b) the proposed scheme.

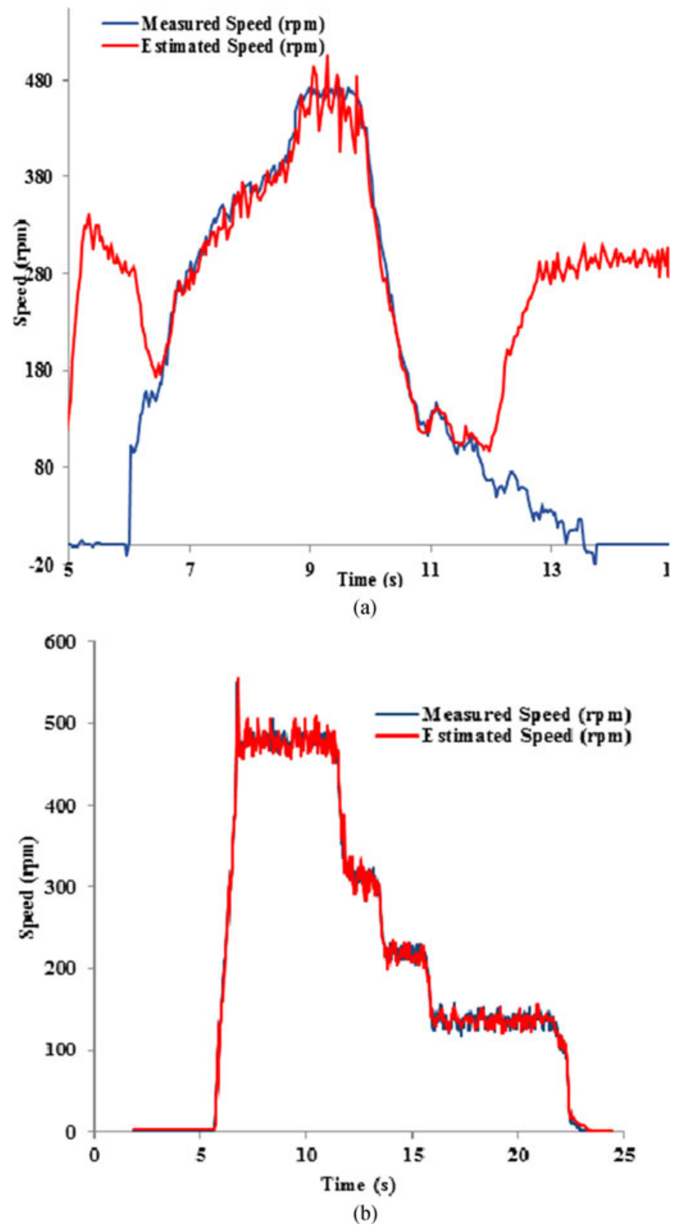

Fig. 8. Experimental results for sensorless performance with 50% increase in the stator resistance at 15 Nm. (a) Conventional Back-EMF MRAS (b) the proposed scheme.

this scheme is consistent in starting from standstill and shows no steady-state error at zero speed.

2) Sensitivity to Stator Resistance Variation: This test was carried out to demonstrate robustness of the proposed scheme against sensitivity to the stator resistance variations. During this test, the stator resistance was increased by 50% and 100% from its nominal value and the applied torque command was kept constant at 15 Nm. Results for the conventional scheme are shown in Figs. 8(a) and 9(a) for cases of 50% and 100% increase in the stator resistance value, respectively. It is clear that, in the case of 50% increase, this scheme suffers from sensitivity to stator resistance variations at low speeds and it becomes more unstable for the case of 100% increase. Results of the proposed scheme are shown in Figs. 8(b) and 9(b) for 50% and 100% increase in the stator resistance value, respectively. It is obvious that the estimated speed continuous tracking the measured speed regardless of 50% or 100% increase in the stator resistance value. Hence, the proposed scheme is robust against sensitivity to the stator resistance variations.

3) Constant Speed Operation at Different Torque Levels: This test was carried out to demonstrate the behavior of the proposed scheme at constant speed with load torque variations. For this test, the shaft speed was kept constant at 300 r/min with the applied torque command varied in 5 Nm intervals from 15 to 50 Nm. Results of this test are shown in Fig. 10(a) and (b) for the conventional and proposed schemes, respectively. As can be seen, the conventional scheme has significan

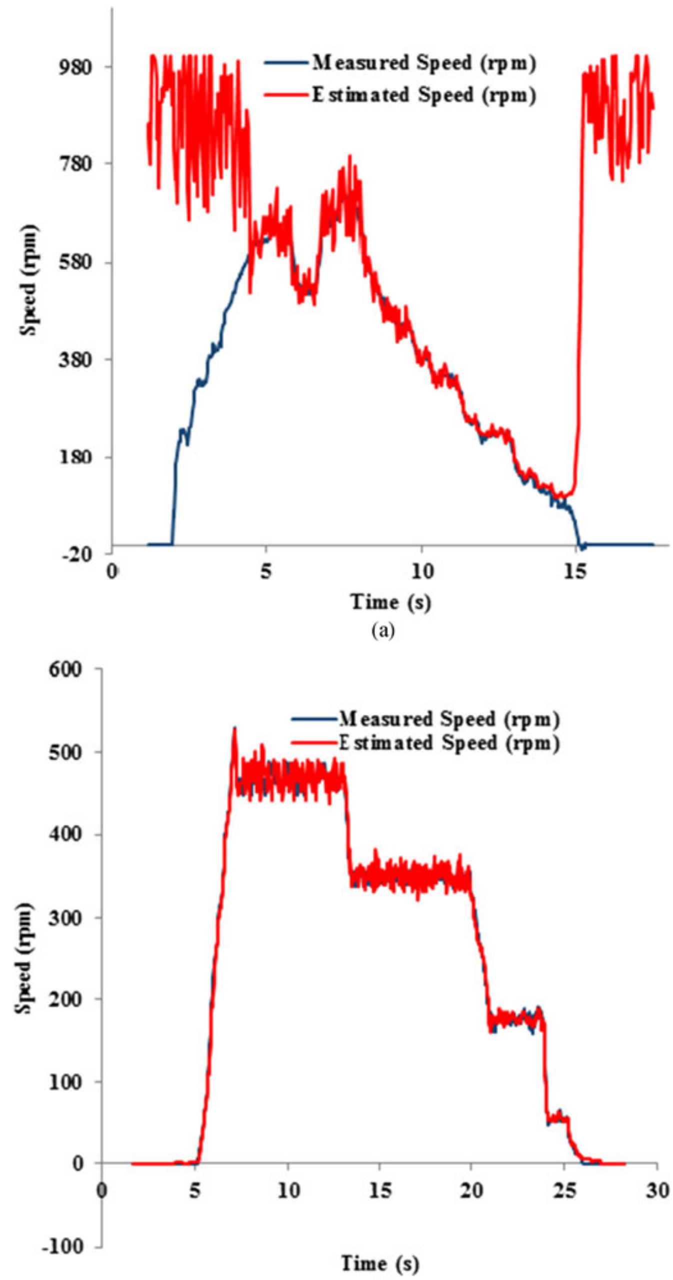

Fig. 9. Experimental results for sensorless performance with 100% increase in the stator resistance at 15 Nm. (a) Conventional Back-EMF MRAS (b) the proposed scheme.

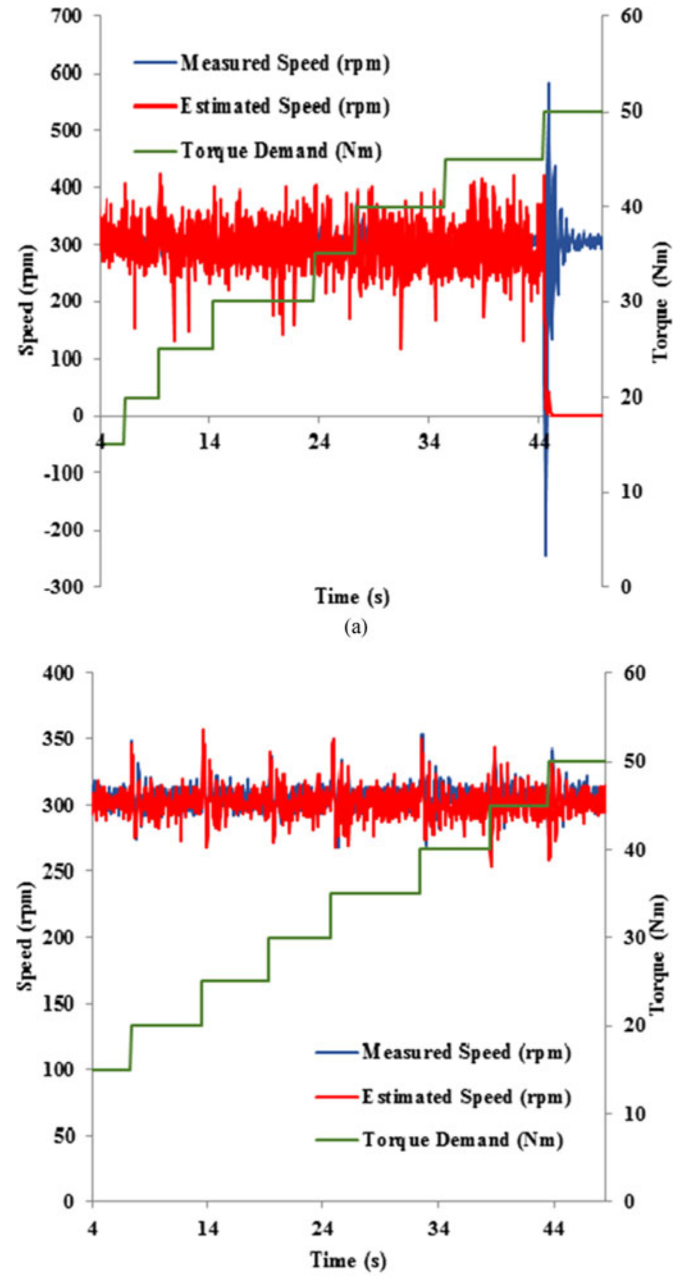

Fig. 10. Experimental results for sensorless performance at constant speed in region of 300 rpm with the torque command increased in 5 Nm intervals from 15 Nm to 50 Nm. (a) Conventional Back-EMF MRAS (b) the proposed scheme.

oscillations and at 50 Nm, it completely loses stability. Hence the estimated speed no longer tracks the measured speed. On the contrary, the proposed scheme shows much less oscillations and the estimated speed continuously tracks the measured speed closely regardless of variations in the torque command level.

B. Experimental Results From Golf Buggy

The following tests were carried out only for the proposed scheme. For these tests, the estimated speed, utilizing the proposed scheme, was employed in the controller instead of the signal from the AB encoder, which was mounted on the vehicle's IM. The speed from the encoder was only used for validation which is labeled as measured speed in the recorded results. During these tests, forward, park, and reverse operation modes were manually selected using the vehicle's gear stick and the torque command was applied using the accelerator pedal.

1) Vehicle Test-Drive for Consecutive Vehicle-Starting From Standstill: This test was carried out to confir the capability of the proposed scheme during consecutive attempts for vehicle starting from standstill in forward and reverse mode directions using the golf buggy.

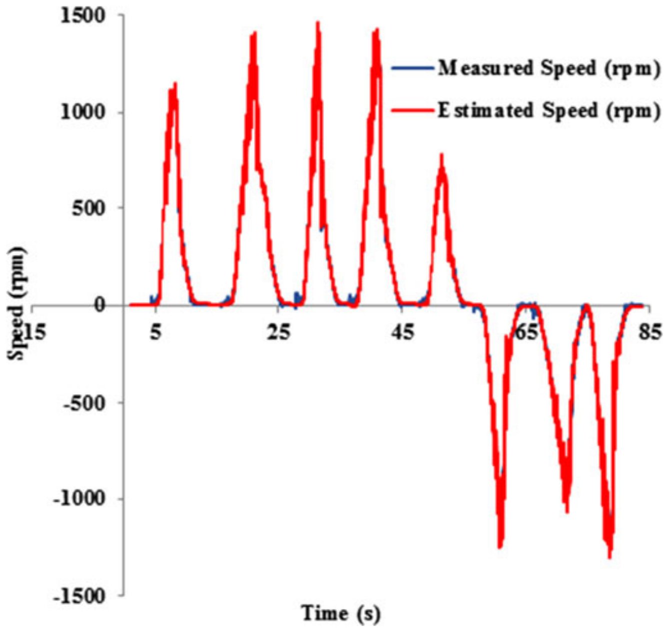

Fig. 11. Experimental result from Golf buggy. Sensorless vehicle-starting from standstill for consecutive attempts in forward and reverse modes of operation.

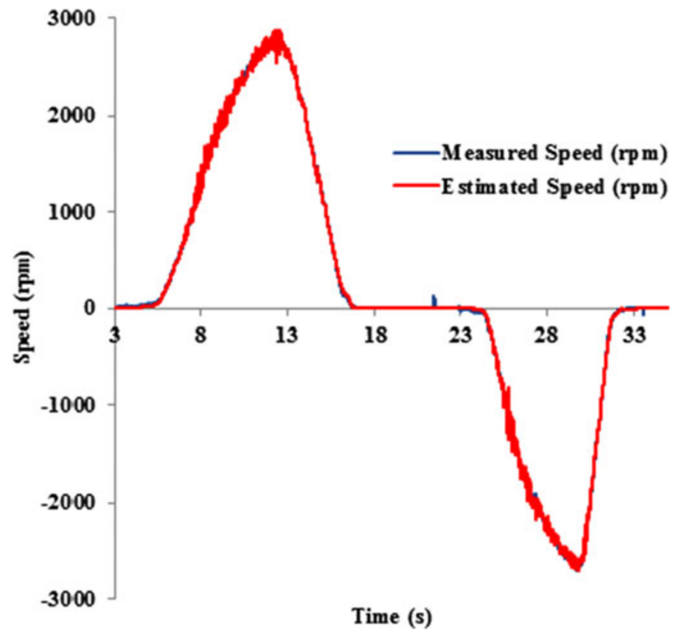

Fig. 12. Experimental result from Golf buggy. Sensorless vehicle test-drive in wide speed range for forward and reverse modes drive operation.

During this test, the vehicle was firs driven forward and suddenly stopped by applying brake pedal, which was repeated for fi e attempts. After changing to the reverse mode, the same procedure was repeated for the reverse direction for three attempts. The result of this test is shown in Fig. 11. It is clear that the estimated speed tracks the measured speed very closely in both directions and despite sudden changes in the vehicle speed, the estimator remains stable and consistent in vehicle starting from standstill.

2) Forward and Reverse Test-Drive in Wide Speed Range: It is required that sensorless schemes used for EV applications be capable of performing in a wide speed range, especially in the fiel weakening region. Therefore, this test was carried out to demonstrate the capability of the proposed scheme for wide range of speeds. During this test, the vehicle was accelerated forward to around +2860 r/min and then slowed down to zero and the same procedure was repeated in the reverse direction for the speed around –2860 r/min.

Fig. 12 shows the result of this test, which confirm the capability and reliability of the proposed scheme across the whole speed range. Moreover, utilizing the proposed scheme provides a smooth test-drive in wide speed range. Note that deeper fiel weakening was prevented due to limited length of the test-track but we have found that, with the static testing, further fiel weakening, approximately twice the base speed, can easily be achieved.

3) Vehicle Hill-Starting Performance: This test was carried out to demonstrate the behavior of the proposed scheme during vehicle hill-starting. In order to create a realistic worst case scenario, this test was carried out after 30 mins of the vehicle test-drive to increase the motor's temperature, hence increase in the stator resistance above its nominal value. A 15º ramp, which is especially designed for the vehicle hill-starting test,

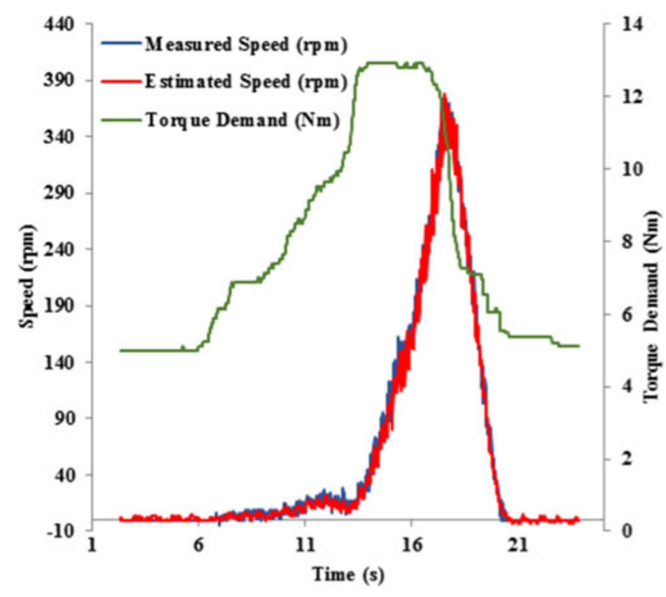

Fig. 13. Experimental result from Golf buggy. Sensorless vehicle test-drive in hill-starting for forward mode drive operation.

was used for purpose of this test. In order to prevent the vehicle from rolling backwards, a torque command of around 5 Nm was initially applied, using the accelerator pedal. The torque command was gradually increased to cause the vehicle to move forward and then the accelerator was gradually eased back to reduce the torque command to around 5 Nm again. The result of this test is shown in Fig. 13, which illustrates stability and reliability of this scheme during the vehicle hill-starting. It is clear that the vehicle did not roll backward during standstill period while it was on the ramp.

VI. Conclusion

A novel Back-EMF MRAS speed estimator is described in this paper for the purpose of sensorless TCD employed for the fault-tolerant limp-home mode EV applications. The proposed scheme was successfully implemented and tested on two different IMs using a laboratory test bench and an EV (a golf buggy), respectively. This scheme is not computationally demanding and is robust against stator resistance variations of 50% and 100% increase. The proposed scheme is not only consistent and stable for the vehicle starting from standstill and low speeds, it also performs reliably above base speed in the fiel weakening region. During the tests, the proposed scheme had shown satisfactory operation throughout forward and backward modes of operation in addition to the constant speed variable load operation. More importantly, the scheme had demonstrated satisfactory performance for vehicle hill-starting. Therefore, the proposed Back-EMF MRAS scheme is suitable for the limp-home mode operation of EV applications by providing consistent, safe, and reliable operation over the whole speed range.

Appendix

TABLE I
Nominal Parameters of IM Used in Experimental Setup

Power [kW]	19	Stator inductance [H]	$2.9811 * 10^{-4}$
DC link voltage [V]	65	Rotor inductance [H]	$2.9810 * 10^{-4}$
Phase voltage [V] (rms)	27	Stator resistance [Ω]	$3.6 * 10^{-3}$
Rated torque [N · m]	100	Rotor resistance [Ω]	$3.1 * 10^{-3}$
Rated frequency [Hz]	52	Magnetizing inductance [H]	$8.85 * 10^{-4}$
Rated current [A] (rms)	450	Number of Pole pairs	2

TABLE II
Nominal Parameters of 5-kW IM for Electric Golf Buggy

Power [kW]	5	Stator inductance [H]	$85.027 * 10^{-4}$
DC link voltage [V]	48	Rotor inductance [H]	$37.344 * 10^{-4}$
Phase voltage [V] (rms)	28	Magnetizing inductance [H]	$7.78 * 10^{-4}$
Rated torque [N · m]	21	Rotor resistance [Ω]	$4.45 * 10^{-3}$
Rated frequency [Hz]	78	Stator resistance [Ω]	$10.24 * 10^{-3}$
Rated current [A] (rms)	138	Number of Pole pairs	2

References

[1] M. E. H. Benbouzid, D. Diallo, and M. Zeraoulia, "Advanced fault-tolerant control of induction-motor drives for EV/HEV traction applications: From conventional to modern and intelligent control techniques," *IEEE Trans. Veh. Technol.*, vol. 56, no. 2, pp. 519–528, Mar. 2007.

[2] D. Diallo, M. E. H. Benbouzid, and A. Makouf, "A fault-tolerant control architecture for induction motor drives in automotive applications," *IEEE Trans. Veh. Technol.*, vol. 53, no. 6, pp. 1847–1855, Nov. 2004.

[3] D. O. Neacsu and K. Rajashekara, "Comparative analysis of torque-controlled IM drives with applications in electric and hybrid vehicles," *IEEE Trans. Power Electron.*, vol. 16, no. 2, pp. 240–247, Mar. 2001.

[4] I. M. Alsofyani and N. R. N. Idris, "Simple flu regulation for improving state estimation at very low and zero speed of a speed sensorless direct torque control of an induction motor," *IEEE Trans. Power Electron.*, vol. 31, no. 4, pp. 3027–3035, Apr. 2016.

[5] D. Casadei, F. Profumo, G. Serra, and A. Tani, "FOC and DTC: Two viable schemes for induction motors torque control," *IEEE Trans. Power Electron.*, vol. 17, no. 5, pp. 779–787, Sep. 2002.

[6] V. S. S. P. K. Hari and G. Narayanan, "Theoretical and experimental evaluation of pulsating torque produced by induction motor drives controlled with advanced bus-clamping pulse width modulation," *IEEE Trans. Ind. Electron.*, vol. 63, no. 3, pp. 1404–1413, Mar. 2016.

[7] K. B. Lee and F. Blaabjerg, "Sensorless DTC-SVM for induction motor driven by a matrix converter using a parameter estimation strategy," *IEEE Trans. Ind. Electron.*, vol. 55, no. 2, pp. 512–521, Feb. 2008.

[8] J. Holtz, "Sensorless control of induction motor drives," *Proc. IEEE*, vol. 90, no. 8, pp. 1359–1394, Aug. 2002.

[9] Y. Zhong-gang, Z. Chang, Z. Yan-ru, and L. Jing, "Research on robust performance of speed-sensorless vector control for the induction motor using an interfacing multiple-model extended kalman filter" *IEEE Trans. Power Electron.*, vol. 29, no. 6, pp. 3011–3019, Jun. 2014.

[10] S. A. Davari, D. A. Khaburi, F. Wang, and R. M. Kennel, "Using full order and reduced order observers for robust sensorless predictive torque control of induction motors," *IEEE Trans. Power Electron.*, vol. 27, no. 7, pp. 3424–3433, Jul. 2012.

[11] S. Di Gennaro, J. R. Dominguez, and M. A. Meza, "Sensorless high order sliding mode control of induction motors with core loss," *IEEE Trans. Ind. Electron.*, vol. 61, no. 6, pp. 2678–2689, Jun. 2014.

[12] A. K. Abdelsalam, M. I. Masoud, M. S. Hamad, and B. W. Williams, "Improved sensorless operation of a csi-based induction motor drive: Long feeder case," *IEEE Trans. Power Electron.*, vol. 28, no. 8, pp. 4001–4012, Aug. 2013.

[13] A. V. R. Teja, V. Verma, and C. Chakraborty, "A new formulation of reactive-power-based model reference adaptive system for sensorless induction motor drive," *IEEE Trans. Ind. Electron.*, vol. 62, no. 11, pp. 6797–6808, Nov. 2015.

[14] M. Cirrincione, A. Accetta, M. Pucci, and G. Vitale, "MRAS Speed Observer for High-Performance linear induction motor drives based on linear neural networks," *IEEE Trans. Power Electron.*, vol. 28, no. 1, pp. 123–134, Jan. 2013.

[15] S. M. Gadoue, D. Giaouris, and J. W. Finch, "Sensorless control of induction motor drives at very low and zero speeds using neural network flu observers," *IEEE Trans. Ind. Electron.*, vol. 56, no. 8, pp. 3029–3039, Aug. 2009.

[16] B. Wang, Y. Zhao, Y. Yu, G. Wang, D. Xu, and Z. Dong, "Speed-sensorless induction machine control in the field-wea ening region using discrete speed-adaptive full-order observer," *IEEE Trans. Power Electron.*, vol. 31, no. 8, pp. 5759–5773, Aug. 2016.

[17] S. M. Gadoue, D. Giaouris, and J. W. Finch, "MRAS sensorless vector control of an induction motor using new sliding-mode and fuzzy-logic adaptation mechanisms," *IEEE Trans. Energy Convers.*, vol. 25, no. 2, pp. 394–402, Jun. 2010.

[18] J. W. Finch and D. Giaouris, "Controlled AC electrical drives," *IEEE Trans. Ind. Electron.*, vol. 55, no. 2, pp. 481–491, Feb. 2008.

[19] C. Schauder, "Adaptive speed identificatio for vector control of induction motors without rotational transducers," *IEEE Trans. Ind. Appl.*, vol. 28, no. 5, pp. 1054–1061, Sep./Oct. 1992.

[20] M. Rashed and A. F. Stronach, "A stable back-EMF MRAS-based sensorless low-speed induction motor drive insensitive to stator resistance variation," *IEE Proc.—Elect. Power Appl.*, vol. 151, no. 6, pp. 685–693, Nov. 2004.

[21] F. Z. Peng and T. Fukao, "Robust speed identificatio for speed-sensorless vector control of induction motors," *IEEE Trans. Ind. Appl.*, vol. 30, no. 5, pp. 1234–1240, Sep./Oct. 1994.

[22] T. Orlowska-Kowalska and M. Dybkowski, "Stator-current-based MRAS estimator for a wide range speed-sensorless induction-motor drive," *IEEE Trans. Ind. Electron.*, vol. 57, no. 4, pp. 1296–1308, Apr. 2010.

[23] Y. B. Zbede, S. M. Gadoue, and D. J. Atkinson, "Model predictive MRAS estimator for sensorless induction motor drives," *IEEE Trans. Ind. Electron.*, vol. 63, no. 6, pp. 3511–3521, Jun. 2016.

[24] A. N. Smith, S. M. Gadoue, and J. W. Finch, "Improved rotor flu estimation at low speeds for torque MRAS-based sensorless induction motor drives," *IEEE Trans. Energy Convers.*, vol. 31, no. 1, pp. 270–282, Mar. 2016.

[25] I. Benlaloui, S. Drid, L. Chrifi-Alaoui and M. Ouriagli, "Implementation of a new MRAS speed sensorless vector control of induction machine," *IEEE Trans. Energy Convers.*, vol. 30, no. 2, pp. 588–595, 2015.

[26] F. Wang *et al.* "Finite control set model predictive torque control of induction machine with a robust adaptive observer," *IEEE Trans. Ind. Electron.*to be published.

[27] M. N. Marwali and A. Keyhani, "A comparative study of rotor flu based MRAS and back EMF based MRAS speed estimators for speed sensorless vector control of induction machines," in *Proc. 32nd IAS Annu. IEEE Ind. Appl. Conf.*, pp. 160–166 vol. 1.

[28] A. R. Haron and N. R. N. Idris, "Simulation of MRAS-based speed sensorless estimation of induction motor drives using MATLAB/SIMULINK," in *Proc. IEEE Int. Power Energy Conf.*, 2006, pp. 411–415.

[29] G. Shen, W. Yao, B. Chen, K. Wang, K. Lee, and Z. Lu, “Automeasurement of the Inverter output voltage delay curve to compensate for inverter nonlinearity in sensorless motor drives,” *IEEE Trans. Power Electron.*, vol. 29, no. 10, pp. 5542–5553, Oct. 2014.

[30] D. P. Marcetic, I. R. Krcmar, M. A. Gecic, P. R. Matic, “Discrete rotor flu and speed estimators for high-speed shaft-sensorless IM drives,” *IEEE Trans. Ind. Electron.*, vol. 61, no. 6, pp. 3099–3108, Jun. 2014.

[31] M. F. Iacchetti, G. D. Marques, and R. Perini, “Torque ripple reduction in a DFIG-DC system by resonant current controllers,” *IEEE Trans. Power Electron.*, vol. 30, no. 8, pp. 4244–4254, Aug. 2015.

[32] L. Zhao, J. Huang, J. Chen, and M. Ye, “A parallel speed and rotor time constant identificatio scheme for indirect fiel oriented induction motor drives,” *IEEE Trans. Power Electron.*, vol. 31, no. 9, pp. 6494–6503, Sep. 2015.

[33] D. Stoji, M. Milinkovi, S. Veinovi, I. Klasni, “Improved stator flu estimator for speed sensorless induction motor drives,” *IEEE Trans. Power Electron.*, vol. 30, no. 4, pp. 2363–2371, Apr. 2015.

[34] G. F. Franklin, J. D. Powell, and A. Emami-Naeini, *Feedback Control of Dynamic Systems*, 6th ed., Upper Saddle River, NJ, USA: Pearson, 2010, pp. 654–660.

Ehsan Dehghan-Azad (S’16) received the B.Eng. degree in electrical and electronic engineering from Newcastle University, Newcastle upon Tyne, U.K., in 2014. Since 2014, he has been working toward the Ph.D. degree in electrical engineering at Newcastle University.

His research interests include electrical machine drives and control for electric vehicle applications.

Shady Gadoue received the B.Sc. and M.Sc. degrees from Alexandria University, Alexandria, Egypt, in 2000 and 2003, respectively, and the Ph.D. degree from Newcastle University, Newcastle upon Tyne, U.K., in 2009, all in electrical engineering.

From 2009 to 2011, he was an Assistant Professor in the Department of Electrical Engineering, Alexandria University, where he was an Assistant Lecturer from 2000 to 2005. In 2011, he joined the Electrical Power Research Group, Newcastle University, as a Lecturer in control systems. Since March 2016, He has been a Visiting Member of academic staff with the Control and Power Research Group, Imperial College London, London, U.K. His main research interests include control, state and parameter identification and optimization algorithms applied to energy conversion, and power electronic systems.

David Atkinson received the B.Sc. degree in electrical and electronic engineering from Sunderland Polytechnic, Sunderland, U.K., in 1978, and the Ph.D. degree in induction motor control from Newcastle University, Newcastle upon Tyne, U.K., in 1991.

He is a Senior Lecturer with the Electrical Power Research Group, School of Electrical and Electronic Engineering, Newcastle University. He joined the university in 1987 after 17 years in industry with NEI Reyrolle, Ltd., Hebburn, U.K., and British Gas Corporation, Cramlington, U.K. His research interests include control of power electronics systems including electric drives and converters for renewable energy systems.

Dr. Atkinson is a Chartered Electrical Engineer in the U.K. He was the recipient of the Power Premium awarded by the Institution of Electrical Engineers (IEE), U.K.

Howard Slater received the Ph.D. degree in the fiel of motor control from Newcastle University, Newcastle upon Tyne, U.K., in 1996.

He was with Marconi, Rolls-Royce Control Systems, and Nidec (Switched Reluctance Drives). Since 2004, he has been with Sevcon Ltd., specialising in motor control, and is currently the Head of Research. He has several patents in the fiel of motor control.

Peter Barrass received the M.S. degree in electrical and electronic engineering from Leeds University, Leeds, U.K., in 1989, and the Ph.D. degree from Newcastle University, Newcastle upon Tyne, U.K., in 1996, on the subject of high performance switched reluctance drives.

His firs employer was GEC TDPL (now ALSTOM), where he worked on various aspects of high voltage dc transmission, static VAR compensators, naval and rail traction power systems. He joined Control Techniques in 1995, where he worked on the successful unidrive range of variable speed drives, becoming the Power Design Manager in 1999. In 2003, he joined Sevcon Ltd., as the Vice President of engineering. He has authored and co-authored several papers and a book on the subject of power electronics, drives and motor control. He holds several patents.

Dr. Barrass is a member of the IET. Outside work, he likes to spend time with his family and keeping fi cycling and walking.

Frede Blaabjerg (S’86–M’88–SM’97–F’03) received the Ph.D. degree in electrical engineering from Aalborg University, Aalborg, Denmark, in 1992.

He was with ABB-Scandia, Randers, Denmark, from 1987 to 1988. He became an Assistant Professor in 1992, an Associate Professor in 1996, and a Full Professor of power electronics and drives in 1998. His current research interests include power electronics and its applications, such as in wind turbines, PV systems, reliability, harmonics, and adjustable speed drives.

Dr. Blaabjerg has received 17 IEEE Prize Paper Awards, the IEEE PELS Distinguished Service Award in 2009, the EPE-PEMC Council Award in 2010, the IEEE William E. Newell Power Electronics Award 2014, and the Villum Kann Rasmussen Research Award 2014. He was an Editor-in-Chief of the IEEE TRANSACTIONS ON POWER ELECTRONICS from 2006 to 2012. He is nominated in 2014 and 2015 by Thomson Reuters to be between the most 250 cited researchers in engineering in the world.